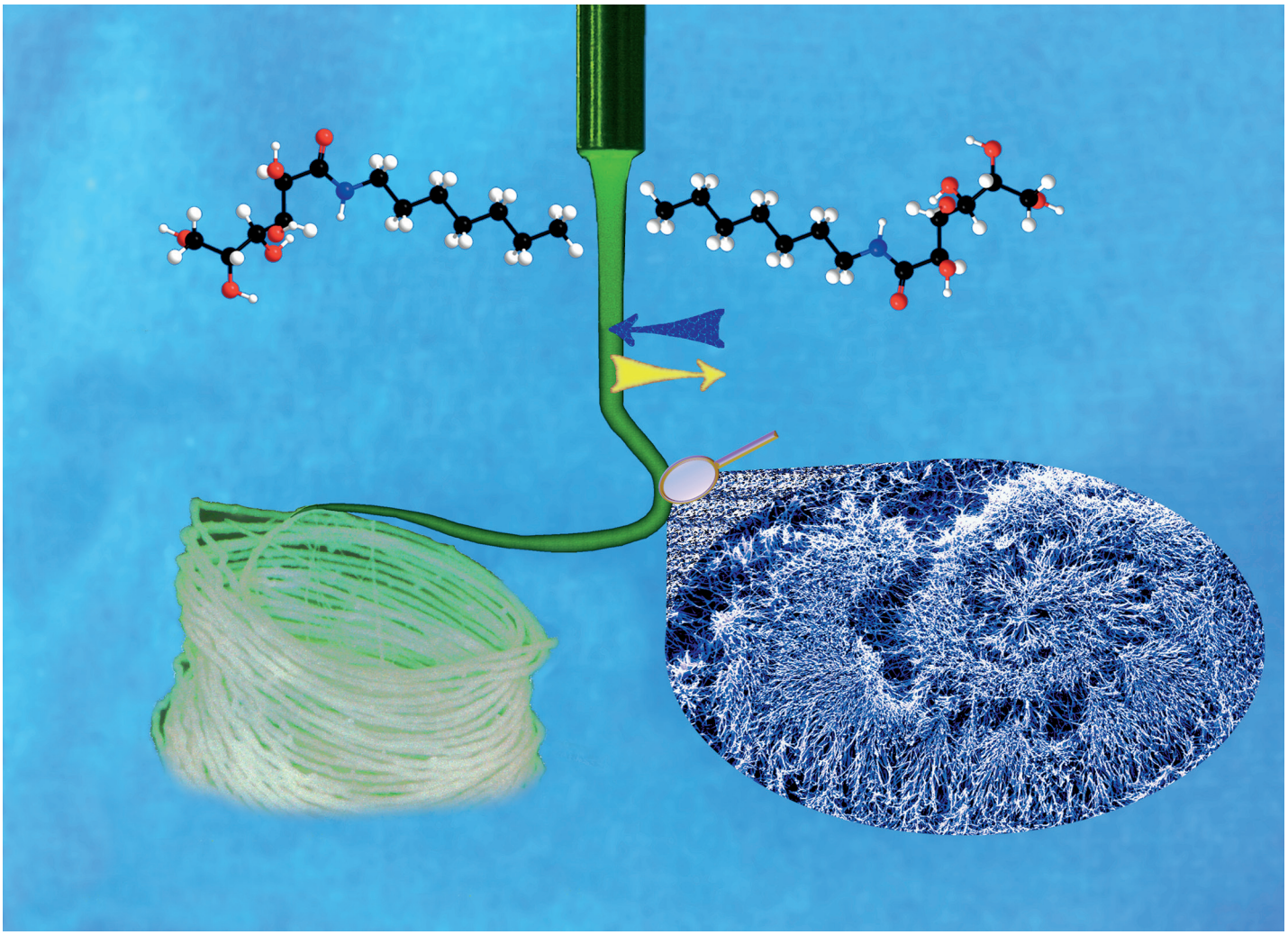

Showcasing research from Dr Juliette FITREMANN, IMRCP, in partnership with LAAS-CNRS and TONIC-INSERM, University of Toulouse, France.

Wet spinning and radial self-assembly of a carbohydrate low molecular weight gelator into well organized hydrogel filaments

A single biocompatible small molecule, the *N*-heptyl-D-galactonamide can be spun into well-defined hydrogel filaments. A solution of this molecule in dimethylsulfoxide is injected in water, resulting in the formation of a continuous filament. The counter-diffusion of water and dimethylsulfoxide triggers the self-assembly of the molecule into supramolecular nanofibers. A radial organization of the fibers was observed in the gel filaments. This method could be used for making well-defined cell culture scaffolds.

As featured in:

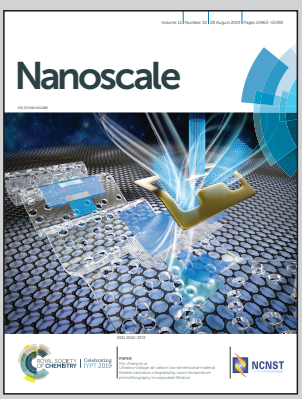

See Juliette Fitremann *et al.*, *Nanoscale*, 2019, **11**, 15043.

ROYAL SOCIETY OF CHEMISTRY | Celebrating IYPT 2019

rsc.li/nanoscale

Registered charity number: 207890

Nanoscale

PAPER

View Article Online
View Journal | View Issue

Cite this: *Nanoscale*, 2019, **11**, 15043

Wet spinning and radial self-assembly of a carbohydrate low molecular weight gelator into well organized hydrogel filaments†

Anaïs Chalard,[a,b] Pierre Joseph,[b] Sandrine Souleille,[b] Barbara Lonetti,[a] Nathalie Saffon-Merceron,[c] Isabelle Loubinoux,[d] Laurence Vaysse,[d] Laurent Malaquin[b] and Juliette Fitremann*[a]

In this work, we describe how a simple single low molecular weight gelator (LMWG) molecule – *N*-heptyl-D-galactonamide, which is easy to produce at the gram scale – is spun into gel filaments by a wet spinning process based on solvent exchange. A solution of the gelator in DMSO is injected into water and the solvent diffusion triggers the supramolecular self-assembly of the *N*-heptyl-D-galactonamide molecules into nanometric fibers. These fibers entrap around 97% of water, thus forming a highly hydrated hydrogel filament, deposited in a well organized coil and locally aligned. This self-assembly mechanism also leads to a very narrow distribution of the supramolecular fiber width, around 150 nm. In addition, the self-assembled fibers are oriented radially inside the wet-spun filaments and at a high flow rate, fibers are organized in spirals. As a result, this process gives rise to a high control of the gelator self-assembly compared with the usual thermal sol–gel transition. This method also opens the way to the controlled extrusion at room temperature of these very simple, soft, biocompatible but delicate hydrogels. The gelator concentration and the flow rates leading to the formation of the gel filaments have been screened. The filament diameter, its internal morphology, the solvent exchange and the velocity of the jet have been investigated by video image analysis and electron microscopy. The stability of these delicate hydrogel ropes has been studied, revealing a polymorphic transformation into macroscopic crystals with time under some storage conditions. The cell viability of a neuronal cell line on the filaments has also been estimated.

Received 29th March 2019,
Accepted 8th May 2019

DOI: 10.1039/c9nr02727k

rsc.li/nanoscale

Introduction

In the context of tissue engineering, we are interested in the development of Low Molecular Weight Gelators (LMWGs or simply molecular gelators) based on saccharides as scaffolds for cell culture. They form a family of materials currently emerging for cell culture, opening the way to innovative approaches in this field. These soft materials are not based on polymers but on the self-assembly of small molecules. The self-assembly phenomenon provides fibrillary structures that entrap water and result in the formation of gels (Fig. 1). Since the self-assembly results from low energy interactions (hydrogen bonds, hydrophobic interactions, π–π stacking, *etc.*), the stability, the mechanical properties, the amount of molecules released and the clearance are different from those of polymers. Also, the self-assembly leads to a wide diversity of fibrillary organizations that are not observed with polymers. Yet it has been shown that the structure of these fibers at the micrometric/nanometric scale has an impact on the behavior of the cells seeded in these gels.[1,2] Several LMWGs are suitable for cell culture.[3–8] Most of them are based on peptides, but other families of LMWGs are also promising for these applications, based on carbohydrates,[2,9–16] nucleosides[17–23] or other building blocks.[24] Our objective was to explore some of the simplest members of this family, for cell culture applications and also for other applications in materials chemistry.

In this context, we recently showed that a very simple synthetic molecule of a low molecular weight, the *N*-heptyl-D-galactonamide (Gal-C7, M.W. 293) – which is easy to produce at the gram scale – provided good results for the culture of a

[a]*IMRCP, Université de Toulouse, CNRS, Bat 2R1, 118 Route de Narbonne, 31062 Toulouse Cedex 9, France. E-mail: fitreman@chimie.ups-tlse.fr*
[b]*LAAS-CNRS, Université de Toulouse, CNRS, UPS, Toulouse, France*
[c]*Université de Toulouse, UPS and CNRS, ICT FR2599, 118 route de Narbonne, 31062 Toulouse, France*
[d]*TONIC, Toulouse NeuroImaging Center, Université de Toulouse, Inserm, UPS, France*

†Electronic supplementary information (ESI) available: Jet velocity analysis and fiber width distribution histograms; thermogravimetric analysis; and SAXS, WAXS and RX. See DOI: 10.1039/c9nr02727k

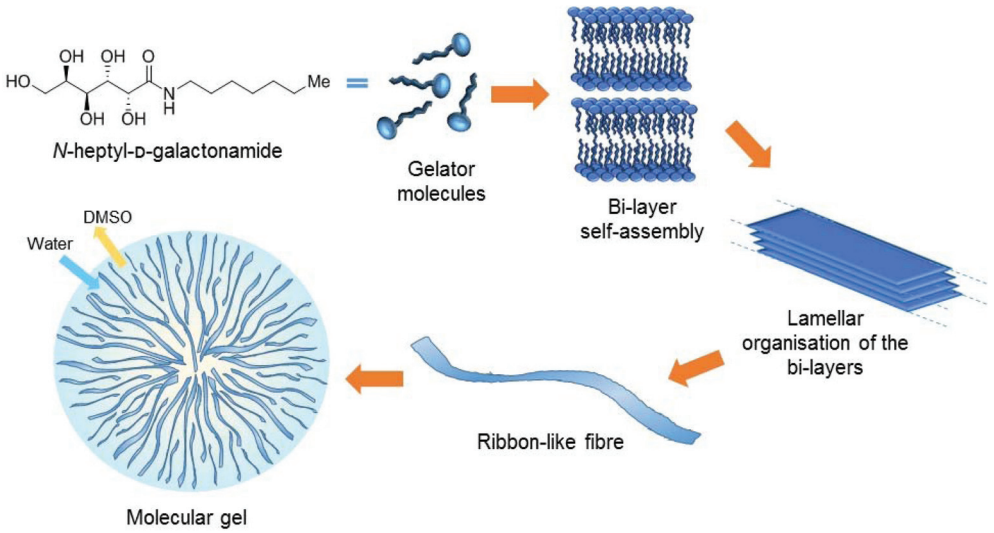

Fig. 1 Structure of the Gal-C7 molecule and the self-assembly mechanism.

neuronal cell line (Neuro2A) and adult human neural stem cells (hNSCs).[2] It has been related notably to the very low rigidity of these gels, which is known to be suitable for the growth and differentiation of neuronal cells.[25] Still in the context of neuronal cell culture, it has been shown that oriented scaffolds are able to guide the development of neurites and axons in one preferential direction and can help in a suitable tissue reconstruction.[26–28] Thus, for the scaffolding purpose, and also more generally for extending the scope of LMWG applications, our objective was to explore how fluidics (or microfluidics) can drive the self-assembly of the gelator into well-defined structures and shapes.

In the context of LMWGs, examples that tackle the control of self-assembly by using external fields still remain scarce. Applying well-controlled external triggers should bring interesting self-assembling effects and may result in new kinds of self-assembled materials with more controlled properties. Some studies described the use of shear stress,[26,29–33] controlled reagent exchanges in microfluidic devices,[34–38] electrical[39] or magnetic fields,[40,41] surface effects[42–44] or ice growth[45] to control self-assembly. While microfluidics is often used to control the self-assembly of micelles, particles, liquid crystals and some polymers,[46,47] it is scarcely the case for molecular gels. Concerning the Gal-C7 hydrogel, the direct shearing of the gel to promote alignment was not possible because this kind of gel undergoes strong synaeresis when a mechanical stress is applied. For this reason, we explored a different way to work with this hydrogel.

Despite its galactonamide polar head and a quite short alkyl chain, the Gal-C7 molecule has very low solubility in water. It appeared that it might be possible to take advantage of this low solubility to trigger the self-assembly of the molecules by precipitation in water under controlled conditions. This principle is used for polymers in the technique of wet spinning. It consists in dissolving a polymer in a good solvent (this solution is called the "dope") and extruding it into a non-solvent (called the "coagulation bath") that triggers the precipitation of the polymer by counter diffusion. Wet spinning has regained interest recently for the production of fibers made out of biocompatible polymers such as collagen,[48] poly(L-lactic acid)[49] or polycaprolactone,[50] alginate,[51] chitosan,[52–54] silkworm[55] or spider silk,[56,57] and notably for tissue engineering applications. Another advantage of wet spinning is that it can be scaled down to microfluidic systems in order to form micrometric or even nanometric yarns; and also to achieve different structures and organizations of the fibers: hollow, multi-component, grooved or even coded fibers can be fabricated by using the right types and layout of channels.[58] Furthermore, wet spinning can be adapted to additive manufacturing and 3D printing techniques, through the precise deposition of the wet-spun fibers in three dimensions.[59,60] Despite the use of the solvent exchange principle for preparing "bulk" molecular gels,[61] very scarce examples describe the use of this physicochemical principle to spin fibers of supramolecular materials and non-polymeric "small" molecules while triggering their self-assembly. One study deals with the self-assembly by wet spinning of emulsion droplets charged with a copolymer.[62] Otherwise few studies implemented electrospinning techniques for spinning small molecules without a polymer carrier (and without a coagulation bath), such as non-polymer liquid crystals,[63] self-assembling peptides,[64,65] tannic acid,[66] cyclodextrins[67,68] or lipids.[69] In these cases, fibers made of the pure compound, thus, which are not gels, are obtained.

In this work we report the production of highly hydrated gel filaments, resulting from the self-assembly of a small molecule by solvent exchange, the *N*-heptyl-D-galactonamide under wet spinning conditions. The influence of the spinning parameters on gelation such as the flow rate, the dope concentration (*i.e.* the concentration of the gelator solution in DMSO) or the needle gauge is studied. The internal microscopic organization

of the gel filaments was investigated by electron microscopy and scattering techniques, showing a well-defined organization of the self-assembled nanometric fibers. The diameters of the dope jet and of the resulting filament, and the velocity of the jet in the coagulation bath have also been investigated. Finally, the stability and the lifespan of the gel filaments were determined under different conditions, revealing polymorphism.

Since the gel itself is formed by the self-assembly of the molecule into nanometric fibers, for the sake of clarity, throughout the rest of the paper, the terms "filament" or "rope" will be used for the fibers of the gel resulting from the wet spinning process. The term "fiber" will stand exclusively for the nanometric fibers resulting from the self-assembly process of the Gal-C7 molecule, structuring the core of the gel filament.

Results and discussion

Application of wet spinning to *N*-heptyl-D-galactonamide

The *N*-heptyl-D-galactonamide (Gal-C7) hydrogels are usually prepared by cooling a 100 °C-heated solution of the gelator, at a typical concentration around 0.5 wt%. Upon cooling, the supramolecular fibers self-assemble (Fig. 1), resulting in a very wide size distribution (see Fig. 7g).[2] Some of these fibers reach a millimetric length and several microns of width. The sol–gel transition occurs at high temperature, around 65 °C, precluding notably the introduction of living matter before setting. In addition, these gels are known to be mechanically very delicate. When a shear stress is applied, the gel undergoes syneaeresis, leading to water expulsion and the formation of a compact fiber mat. For this reason, this gel cannot be injected. To solve both problems, and also to study in a larger context different ways to self-assemble these molecules, we were looking for solutions to trigger the formation of the hydrogel at room temperature by fluidic methods.

The Gal-C7 molecule is soluble in a few organic solvents, including DMSO (dimethylsulfoxide), hexafluoropropanol or methanol, and it is very poorly soluble in water at room temperature. DMSO was first selected because it is the most suited solvent for further biological applications: even though it can be detrimental for cells at high concentrations, it is non-toxic at lower ones and can be easily washed from the gel since it is miscible with water. By dissolving Gal-C7 in DMSO and injecting the solution in water, interestingly, we observed that a continuous filament of gel was produced (Fig. 2). This result was not really expected, since most of the time, the precipitation of a solute into a non-solvent bath leads to discontinuous aggregates. In the case of the Gal-C7 solution, both the properties of the solvent and the self-assembly mechanism promoted the formation of a continuous filament instead of discrete precipitation. As a matter of fact, DMSO is denser than water and it dives into the bath forming a continuous string instead of quickly mixing with water (Fig. 2d).

When extruding the DMSO gelator solution in the water bath, coagulation occurs by solvent exchange by counter

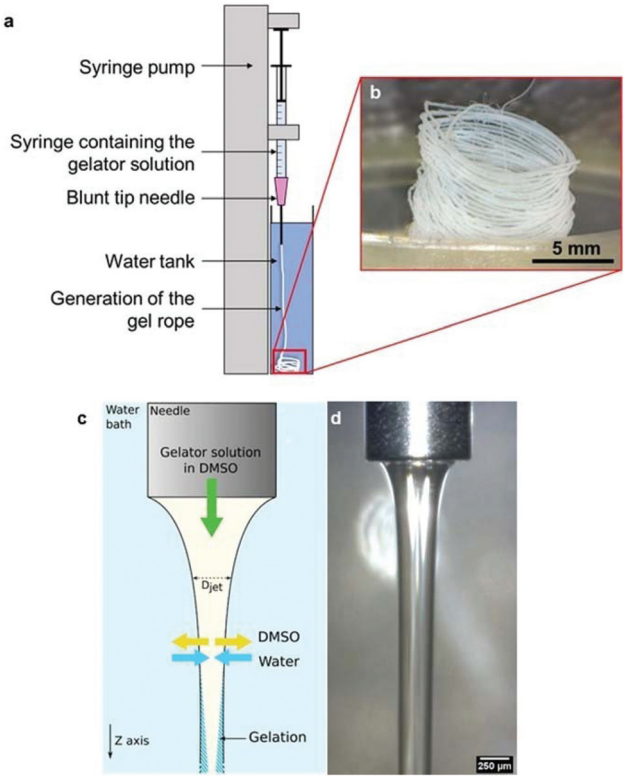

Fig. 2 a. Experimental setup used for the generation of a continuous gel filament. b. Coiled filament of the gel obtained after the extrusion of a 4 wt% Gal-C7 solution in DMSO (50 µl min^{-1}, 20G needle, ID 600 µm). c. Principle of the wet spinning technique: the gelator solution in DMSO is extruded through the syringe and a counter diffusion between DMSO and water occurs, resulting in the progressive gelation of the jet. d. Observation of the DMSO jet after the needle exit (30 µl min^{-1}).

diffusion. When water meets the gelator molecules, it triggers their self-assembly into nanometric fibers that retain water and thus form the hydrogel. Due to a simple effect related to the mechanics of ropes,[70] the gel falling in the solution often wraps in a coil, giving in those cases spontaneously locally aligned filaments.

Conditions for the formation of a continuous filament of the gel

In order to determine the most suited conditions to obtain Gal-C7 filaments, and also to check the robustness of the process, phase diagrams were established by setting the following parameters: the applied flow rate, the concentration of the Gal-C7 solution and the needle gauge. The bath temperature was kept constant at 22 °C (room temperature). The flow rates applied by the syringe pump varied from 0.5 to 200 µL min^{-1}, the solution concentrations from 1.25 to 5 wt% and the needle inner diameters (ID) from 160 to 600 µm (30G to 20G). The phase diagrams were then based on simple visual observations and are presented in Fig. 3 (the different experiments at a given concentration have been slightly shifted from each other for clarity). Three regimes were identified (with a color code given on Fig. 3), separated by two transition regions: (i) the gel forms a clog directly after exiting the needle (red); (ii) a stable

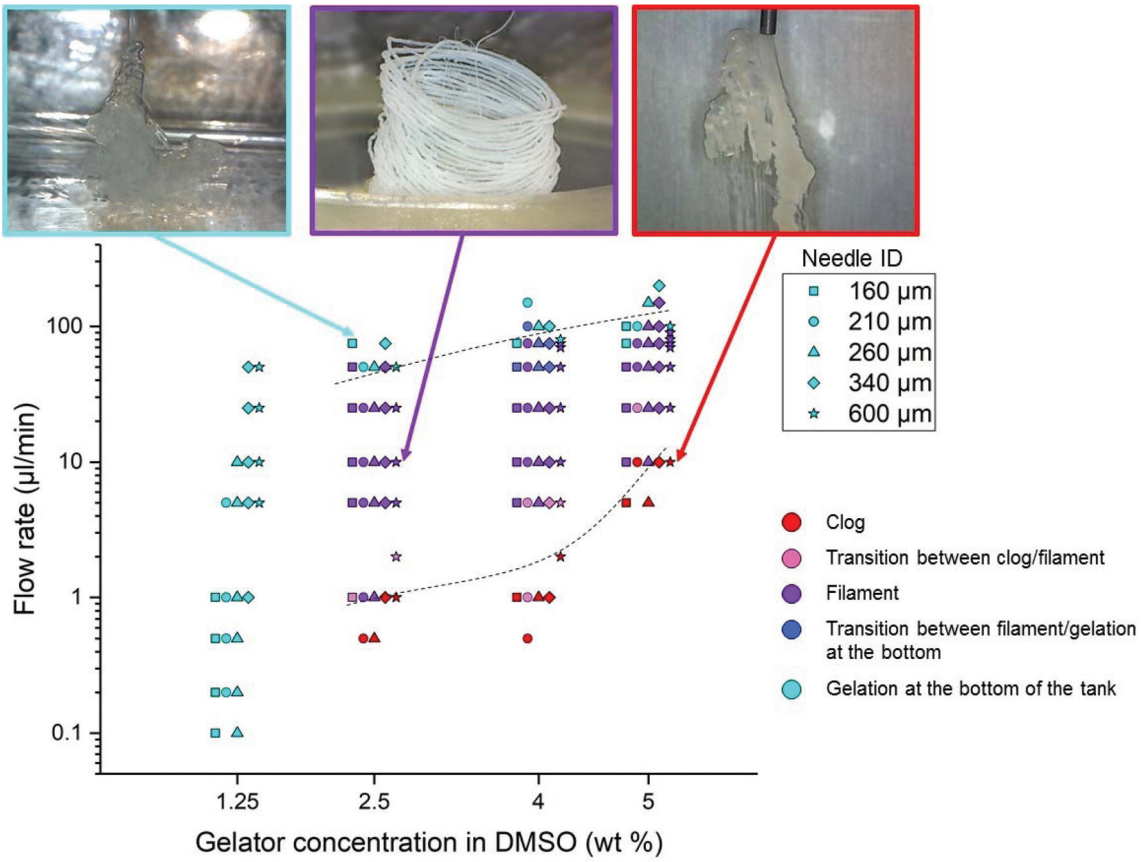

Fig. 3 Flow rate/concentration phase diagrams for the Gal-C7 wet spinning. The different needle inner diameters (see inset for "Needle ID") are represented by different marker shapes (squares, diamonds, stars, *etc.*). On the *X*-axis is represented the different concentrations of the gelator solution in DMSO. All the experiments were performed at precise concentrations (1.25/2.5/4 and 5 wt%), but for displaying the results of these experiments in the same diagram, the markers were slightly shifted from each other. Photographs of the different states of the gel are given on the top (from left to right): gelation at the bottom of the tank; filament of the gel; clog at the exit of the needle.

continuous filament is obtained (purple); and (iii) the gelation does not occur before reaching the bottom of the bath and no filament is formed (light blue). Between these well defined regimes, two transition regions were observed: (iv) a filament is formed but the needle is clogged after a few seconds (pink); and (v) the gelation occurs but to a rather lower extent in the bath (blue).

The main information we extracted from this diagram is as follows. First, it provides the conditions of the concentration and flow rate to obtain the desired continuous gel filaments. They can thus be formed with Gal-C7 concentrations between 2.5 and 5 wt% and flow rates between 5 and 50 μL min^{-1}. When the concentration was too low (1.25 wt%), we were not able to find any condition for which a continuous filament was formed. This result illustrates the fact that a continuous gel filament can be obtained only when the supramolecular fibers are dense enough to be more or less intertwined (see part 4). If the concentration of the molecule is too low, the supramolecular fiber network is too sparse to sustain a continuous string. Secondly, when the concentration increases, a higher flow rate must be applied to avoid clogging. More generally, at any concentration, if the flow rate is too low, a clog tends to form at the exit of the needle. Conversely, when the flow rate is too high, the solution does not have time to gel before reaching the bottom of the bath. These results are directly explained by the contact time of the DMSO/Gal-C7 solution with water. If the flow rate is too slow, water can diffuse early in the DMSO/GalC7 solution, resulting in clogging. If the flow rate is too high, the water does not have the time to diffuse inside the DMSO liquid rope before it reaches the bottom. It means that there is an optimal flow rate window within which the jet speed and the water diffusion match to trigger the gelation into a continuous filament. Concerning the needle diameter, surprisingly, this parameter does not seem to influence much the position of the limits in the diagram.

Characterization of the spinning process

The gelation mechanism and the solvent exchange occurring in the wet spinning process were investigated with different methods.

Characterization of the solvent exchange and the gelation mechanism. In order to highlight the solvent exchange occurring during the extrusion, fluorescence markers were introduced into the GalC7/DMSO solution and tracked with a microscope camera adapted to fluorescence observations. The DMSO diffusing out of the jet throughout the fall and the gelation were characterized with fluorescent beads (1 μm diameter) introduced into the GalC7/DMSO solution. The fluorescent beads are big enough so that they do not diffuse with the DMSO and stay with the gelator inside the jet. Fig. 4a shows the white light (Fig. 4a1), the fluorescence (Fig. 4a2) acquisitions and the resulting image when the two are superimposed (Fig. 4a3). The latter reveals the DMSO surrounding the fluorescent jet (a grey-brown layer) where the gelator and the beads are, especially at the bottom of the picture. This shows that indeed the DMSO diffuses out of the jet into the water bath, and this occurs rather early in the process (1 cm after the exit of the needle). The second experiment aimed at characterizing the diffusion of water inside the jet and the subsequent gelation of the solution. For this purpose, salicylaldehyde azine, which has the ability to form fluorescent aggregates in the presence of water ("aggregation induced emission" or AIE), was used. A fluorescent layer was observed at the edges of the jet and progressively thickened towards the center (Fig. 4b). Since the fluorescence only occurs when the salicylaldehyde azine is exposed to water, this highlights the diffusion of water inside the DMSO jet, and thus the progressive gelation of GalC7 from the edges towards the center of the jet. At the end of the fall, the fluorescence is homogeneous in the filament and the gelation is complete.

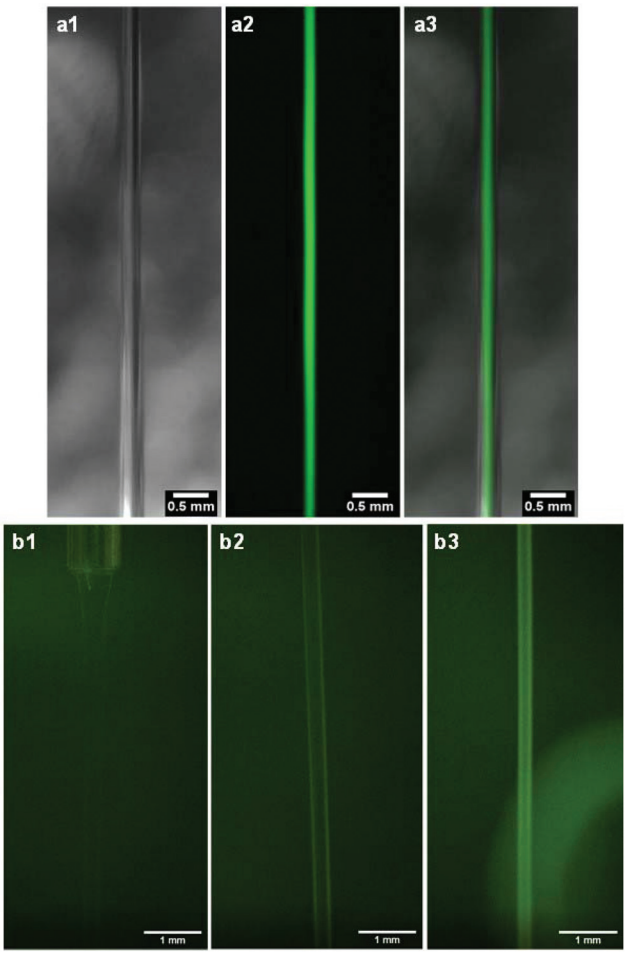

Fig. 4 a1–3: Characterization of the DMSO diffusing out of the forming gel filament ≈1 cm after the needle exit. White light (a1) and fluorescence (a2) observations of the jet and the superimposition of the two pictures (a3). b1–3: Characterization of the water diffusion throughout the fall of the DMSO solution. The pictures were taken at the following distances: 0 cm (b1), ≈3 cm (b2) and ≈6 cm (b3) after the needle exit.

Jet velocity. The velocity of the DMSO jet after exiting the needle was measured. This piece of information is crucial for the potential application of the process to 3D printing, since the printing speed has to be in accordance with the extrusion velocity. These data cannot be simply calculated with the needle section and the flow rate set because the composition of the jet changes along the fall in the bath, due to solvent exchange. To measure the jet velocity, 15 μm fluorescent polystyrene beads were incorporated into the gelator solution and the extrusion was observed with the microscope camera adapted to fluorescence observations (Fig. 5a and c). The beads were big enough to be easily observed with the camera and diluted enough so that they did not disrupt the flow. Only low flow rates were analyzed in order to be able to clearly distinguish the beads individually and measure their velocity while flowing. The jet velocity was measured in the case of a 5 μl min^{-1} flow rate with a 20G needle and a 2.5 wt% gelator solution containing the beads. The measured velocities are presented in Fig. 5b. The jet diameter along the Z axis, namely the profile of the jet, was extracted from the superimposed images of the fluorescent beads (such as the one presented in Fig. 5a) and is reported in Fig. 5d.

What can be seen in Fig. 5b and d is that the velocity of the beads is consistent with the shape of the DMSO jet since the velocity increases as the diameter of the jet decreases. This thinning of the jet is actually due to gravity that pulls the DMSO jet, making it take this hyperbolic shape at the exit of the needle. After a few millimeters, the jet velocity is quasi constant as well as the jet diameter, probably due to a balance between the gravitational force and viscous friction that establishes between the jet and the resting solution surrounding it. The mean jet velocity for a 5 μl min^{-1} flow rate is of 8.3 ± 0.5 mm s^{-1} (see Table SI-1†). The effective flow rate (Q_{eff}) was then calculated from the measured velocities and diameters, thanks to eqn (1):

$$Q_{eff} = v \times S \quad (1)$$

(where Q_{eff} is the effective flow rate, v is the mean measured speed and S is the jet section. The section of the jet was measured from Fig. 5d at the plateau: mean diameter of the jet = 176 μm). As a result, the mean effective flow rate is thus Q_{eff} = 12.6 μl min^{-1}, instead of 5 μl min^{-1}. This difference high-

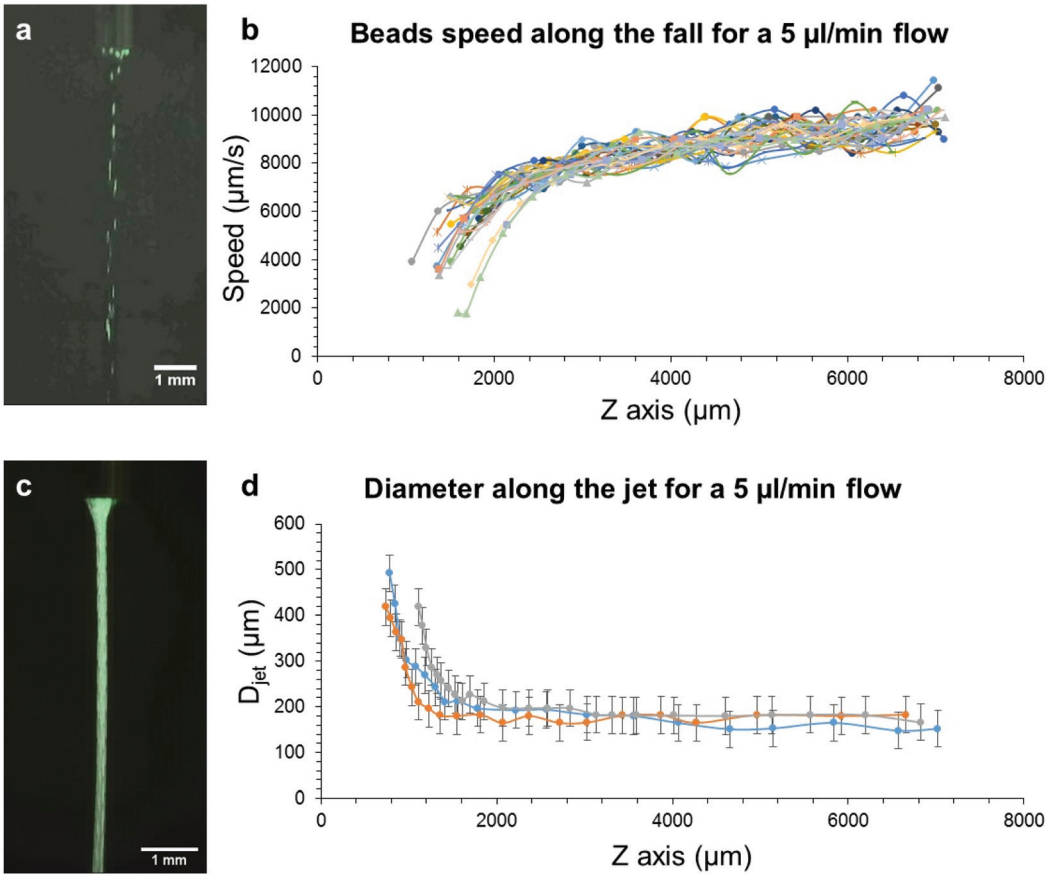

Fig. 5 a. Snapshot of the video acquired to measure the jet speed. b. Speed of the fluorescent beads along their fall with a 5 µl min^{-1} flow rate and a needle ID of 600 µm (20G). c. Mean flow profile obtained from the flow of fluorescent beads in the DMSO/Gal-C7 solution at 5 µl min^{-1} (needle ID: 600 µm, 20G); different frames from the video were superimposed resulting in this image. d. Diameter along the jet measured on the same photograph as c.; three different experiments were performed.

lights that matter is somehow added in the jet during the process, revealing the fact that there is an exchange of the solvent during the spinning and that the composition of the DMSO jet changes along its fall into the bath.

Analyses of the jet and filament diameters. To characterize the wet spinning of Gal-C7 hydrogels, the relationships among the set conditions, the diameters of the DMSO jet and the ones of the final filament were investigated. To do so, the diameter of the DMSO jet and that of the obtained filament were measured under various conditions. The influence of the flow rate and of the needle gauges (20G, ID = 600 µm, orange markers and 27G, ID = 210 µm, blue markers) was evaluated. The solution concentrations also varied, since it was necessary to select conditions of the concentration where a filament is obtained at the flow rate selected (see the phase diagram in Fig. 3). Indeed, at low flow rates, only the less concentrated solution forms a filament and at higher flow rates, a more concentrated one is needed. For each condition, the filament diameter was measured by optical microscopy, as well as the jet diameter at 2.3 mm after the needle exit (maximum distance on the acquired images), thanks to the microscope camera. The results are reported in Fig. 6.

The first thing to note is that, the higher the flow rate, the wider the diameters. Moreover, the resulting gel filament diameter is much smaller than that of the DMSO jet after the needle exit. The needle gauge (orange *versus* blue curves) has a significant influence on the jet diameter (Fig. 6a) but it does not affect the gel filament diameter (Fig. 6b). Actually, the jet diameter is measured very close to the needle exit (2.3 mm after, whereas the total fall height is 80 mm) and at this distance, it is mainly set by the needle size. Different phenomena occur between 2.3 mm and 80 mm: the jet thinning continues slightly after 2.3 mm (Fig. 5d) and the progressive solvent mixing and gel formation may change the volume of the jet. These phenomena may explain the difference in diameters between the jet measured early during the fall and the final gel filament.

What is also noticeable is that the solution concentration does not significantly influence the diameter of the jet since it is possible to build a continuous curve out of the two concentration conditions, 2.5 and 4 wt%. This result tends to show that, at these concentrations in DMSO, Gal-C7 does not induce viscoelastic effects. In the case of the gel filament, this one is slightly thinner with a lower concentration (2.5 wt%) when the

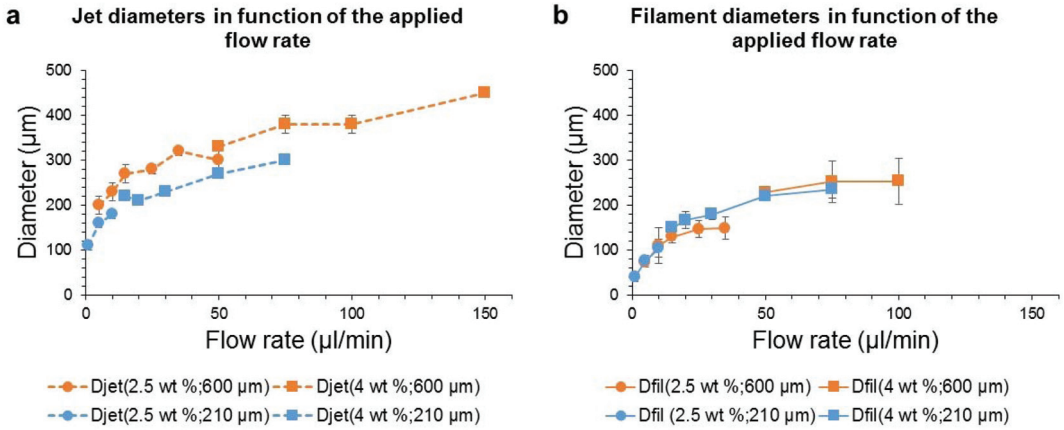

Fig. 6 The jet (a) and the resulting filament diameters (b) were measured for different flow rates and for different needle internal diameters. Two needle gauges were used: 20G (orange) and 27G (blue). Two gelator concentrations in DMSO were also used: 2.5 wt% (circles) and 4 wt% (squares).

smaller needle is used (27G). This difference is amplified when the large needle (20G) is used: a discontinuity between the curves at 2.5 wt% and the curves at 4 wt% is observed. In this case, the more the gelator, the larger the gel filament. However, the effect of the concentration is quite small, showing that the filament and jet diameters seem to be mainly set by the flow rate and by gravity.

Microscopic characterization and composition of the filaments

The microscopic structure of the gel filaments and their composition were studied by optical and electron microscopy and by thermogravimetric analysis.

Optical and electron microscopy observations. The gel filaments can be easily observed with transmission optical microscopy because their size is of several hundreds of micrometers and they are translucent enough to see through (Fig. 7a and b). The constituting fibers of the gel can even sometimes be outlined, especially on the edges of the filaments, and a radial fiber organization is suspected (Fig. 7b). The diameters of the filaments were measured by this technique. For example, in Fig. 7a, the resulting diameter of the fibers is 205 µm and in Fig. 7b it is 180 µm.

The microscopic structure of the wet-spun filaments was further analyzed by cryo-SEM, highlighting the internal organization of the wet-spun gel filaments of Gal-C7 (Fig. 7c–e). They are sustained by a network of supramolecular fibers organized in radially oriented clusters. Interestingly, when the flow rate is high (100 µL min^{-1}), fibers organized in spirals are observed, with a spiral size around 200 µm, matching the filament section (Fig. 7e). The gelator acts as a tracer of the diffusion mechanism during the spinning process. The gel network is also very different from the one obtained in "bulk gels" prepared by cooling down a hot gelator solution in water (Fig. 7g).[2] First, the size of the constituting fibers is much reduced in the case of wet-spun gels compared to that of the bulk ones (Fig. 7g): the mean fiber width is around 140 nm for wet-spun hydrogels whereas the median width for bulk Gal-C7 hydrogels is 1.5 µm. Secondly, the width distribution of the supramolecular fibers: 136 ± 37 nm, is rather narrow in the wet-spun filaments, while in the "bulk gel" a very large distribution: 1.46 ± 2 µm is observed (see Fig. SI-2†). This result shows that the wet spinning enables a high control of the supramolecular fiber formation. Finally, the spatial organization of the fibers in the core of the filament is also striking. There seems to be a general radial organization of the fibers inside the filaments, which can be outlined on the cross section (Fig. 7c) or on the axial section (Fig. 7d), even if not all the fibers follow this pattern. Indeed, this organization results from the radial diffusion of water inside the liquid rope. In Fig. 7d, the edges of a filament can be outlined: the fibers mostly grew perpendicularly to the edge of the filament and go towards its center. As a consequence, the fibers are locally aligned at a microscopic level by this process. The wet spinning techniques thus enable obtaining radially organized supramolecular fibers with a narrow size distribution.

Cryo-SEM also confirmed the filament diameters on some pictures, such as that in Fig. 7a with a diameter around 120 µm, which matches the optical observations.

Thermogravimetric analysis. The ratio of water, DMSO and the gelator in wet-spun Gal-C7 gel filaments was determined by thermogravimetric analyses (TGA) (Fig. SI-3†). The results show that the filament is composed of 3 wt% of Gal-C7 and 97 wt% of water. No remaining DMSO could be detected since no corresponding signal was observed in the thermogram. This result was promising for cell culture applications because the diffusion in the bath during the wet spinning process already significantly decreases the amount of DMSO in the filament.

Lifetime of the wet-spun filaments

Morphological transformation of the filaments into crystals. We earlier observed that the gel filaments formed by the wet spinning process are rather delicate. Actually, they are made of

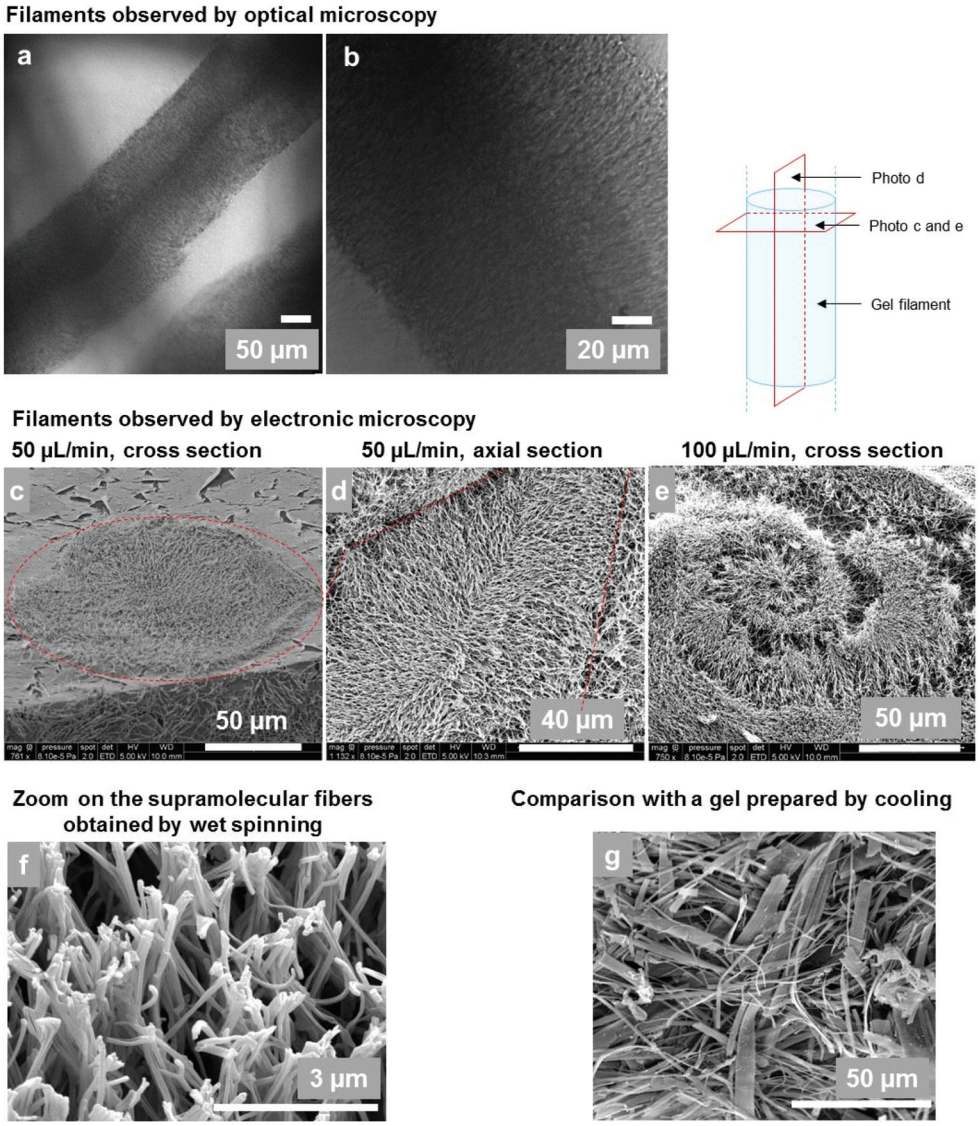

Fig. 7 (a and b) Optical microscopy of gel filaments (4 wt%, 50 µl min^{-1}, 20G needle ID = 600 µm). (c–e) Cryo-SEM observations of gel filament sections. (c) Cross section of a filament (4 wt%, 50 µl min^{-1}, 20G needle). The dotted circle shows the section of the rope. The resulting diameter is around 120 µm. (d) Axial section of a gel filament (5 wt%, 50 µl min^{-1}). The dotted lines show the edges of the filament. The radial arrangement of the supramolecular fibers can be seen. (e) At a higher flow rate (5 wt%, 100 µl min^{-1}), fibers organized in spirals are observed; (f) Supramolecular gel fibers at a higher magnification (5 wt%, 100 µl min^{-1}). (g) For comparison: cryo-SEM of a bulk Gal-C7 gel prepared by cooling down a hot gelator solution in water (0.45 wt%) and not by wet spinning (see ref. 2). Some fiber widths can reach 15 µm.

a hydrogel containing 97% of water, itself sustained by nanometric supramolecular fibers in equilibrium with water. They are resistant when they are manipulated very delicately with a spatula inside the water bath. But they collapse if they are withdrawn out of the bath. Two phenomena were observed: a fast dissolution of the filaments with time when they are kept in a large volume of water (200 mL) and a morphological transformation of these gel filaments into crystals. The lifetime of the filaments and their transformation into crystals were thus determined under different conditions. Their stability in pure water was studied. Also, because of the potential use of these wet-spun filaments for cell culture applications, their lifetimes in DMEM/FBS (Dulbecco's modified Eagle's medium supplemented with 10% of fetal bovine serum) or PBS (Phosphate Buffer Saline) were also studied. For DMEM/FBS, the filaments were kept either at room temperature or at 37 °C. We also observed that the gel ropes, less dense than water, tended to float on top of the liquid and that the contact with air activated the morphological transformation from gel to crystals. The impact of the water–air interface in gel aging has been described for other LMWGs.[71] For this reason, the lifetime was also studied with a cover slip that was placed on top of the liquid. These two different immersion conditions were thus assessed: one with and one without a cover slip on top.

Filaments were spun with a 4 wt% Gal-C7 solution in DMSO, at a flow rate of 50 μl min^{-1} and with a 20G needle. The results are displayed in Table 1 (see also Table SI-4†).

Throughout the days, the filaments vanished progressively and the gelator recrystallized to form macroscopic translucent crystals (Fig. 8). This phenomenon occurred whatever the solution used, except for DMEM/FBS at room temperature where crystals were not observed even after more than a month. Interestingly, DMEM/FBS seems to stabilize the gel filaments for a long time, perhaps because of the numerous solutes of DMEM/FBS, but only at room temperature. Between these two states, spikes on the edges of the filaments can also be observed after some time, as seen in Fig. 8c.

The morphological transformation of low molecular weight gelators into crystals is a phenomenon already known.[72–77] Notably, it has been described for similar molecules belonging to the family of *N*-alkyl-aldonamides.[78] For example *N*-octyl-D-gluconamide, which has a different stereochemistry of the polar head, crystallizes readily. Interestingly, in the case of *N*-heptyl-D-galactonamide, the gels prepared by cooling the hot gelator solutions are stable for months, while the wet-spun gels offer a way to observe this transition.

Table 1 Time for the transformation of the wet-spun Gal-C7 gel filaments into crystals, in days (RT: room temperature)

Conditions	Exposed to air	Under a coverslip
Water (RT)	2	3
PBS (RT)	<1	2
DMEM/FBS (RT)	>34	>34
DMEM/FBS (37 °C)	<1	4

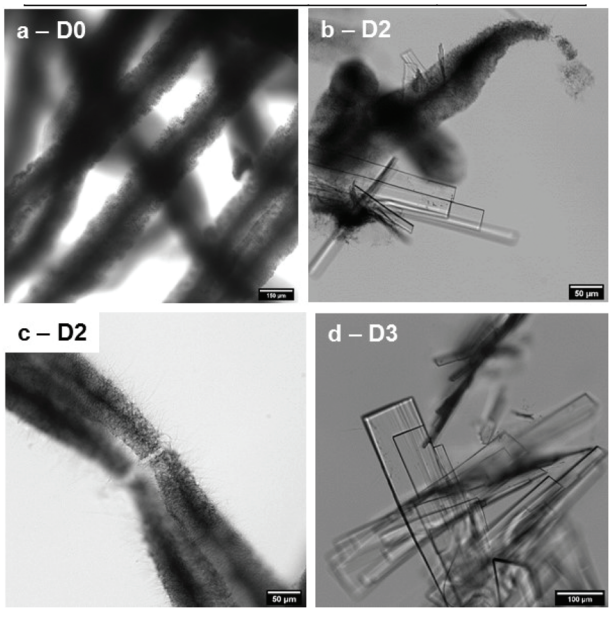

Fig. 8 Evolution of the morphology of Gal-C7 filaments with time in water, without a coverslip: (a) just after extrusion, (b and c) 2 days after extrusion and (d) 3 days after extrusion. Scale bars: 100 μm (a and d) and 50 μm (b and c).

X-Ray analysis of the morphological transformation. The organization of the Gal-C7 molecules in the two morphological states has been studied by small angle X-ray scattering (gel and crystals) and X-ray diffraction (crystals). The SAXS curve for the wet-spun gel is reported in Fig. 9a (see also Fig. SI-5a†) and is indicative of a well defined lamellar organization. The long period spacing of the lamellar structure is d = 35.1 Å and a fiber thickness of 60 nm can been estimated. In the "bulk gel" produced by cooling hot aqueous solutions of the gelator, we described in a preceding paper that the dominant molecular organization of the gelator is also lamellar with a spacing of 35 Å, but a second, less abundant, molecular arrangement with an interaction distance of about 38 Å was also observed.[2] Thus, these results show that the mode of self-assembly of Gal-C7 is mainly the same for the bulk gels and the wet-spun gels, but the wet spinning leads to a better control of the self-assembly since it produces only one kind of spacing.

The crystals obtained from the morphological transformation were also analyzed by SAXS, WAXS and X-ray diffraction. SAXS highlights a lamellar order with a smaller spacing of 30.5 Å (peak position, 0.204 $Å^{-1}$) (Fig. 9a and SI-5b†). The crystallographic structure was determined from X-ray diffraction of bigger crystals (SI-7†). The *N*-heptyl-D-galactonamide (Gal-C7) crystallizes in a monoclinic system (space group $P2_1$). The molecular packing is a symmetric tail-to-tail bilayer sheet comparable to that of the gulonamide[79] and talonamide[80] analogues (Fig. 9b), but is in contrast to the head-to-tail packing observed in the gluconamide analogue.[81] All fatty chains run parallel to each other but quite intriguingly an angle of ~120° is observed between the packed chains at the junction of the tail-to-tail arrangement. An angle of 90 °C has also been described previously in the case of *N*-octyl-D-talonamide.[80] The occurrence of an angle in the packing of the hydrophobic chains has also been been modeled in the case of Fmoc-derived gelators.[82] In the crystal, intermolecular O–H···O and N–H···O hydrogen bonds link the molecules into a three-dimensional network (Fig. SI-7b and Table SI-7†). The stereochemistry of the galactonamide polar head enables the development of a strong hydrogen-bond pattern between hydroxyl groups of adjacent crystal sheets that drives the tail-to-tail molecular packing. In the case of gluconamide, the stereochemistry of the hydroxyl groups is different and leads to a head-to-tail packing. Still for crystals, the WAXS region looks like a powder diffraction spectrum with well defined peaks, while in the case of the gel filament, the same region of the spectrum shows much larger peaks with peak positions different compared with crystals (see Fig. SI-6†). This observation indicates a probable difference in the molecular conformation of the Gal-C7 molecule between the supramolecular fibers and the crystals. Together with the difference in the water content, it may explain the spacing difference between the two kinds of assembly.

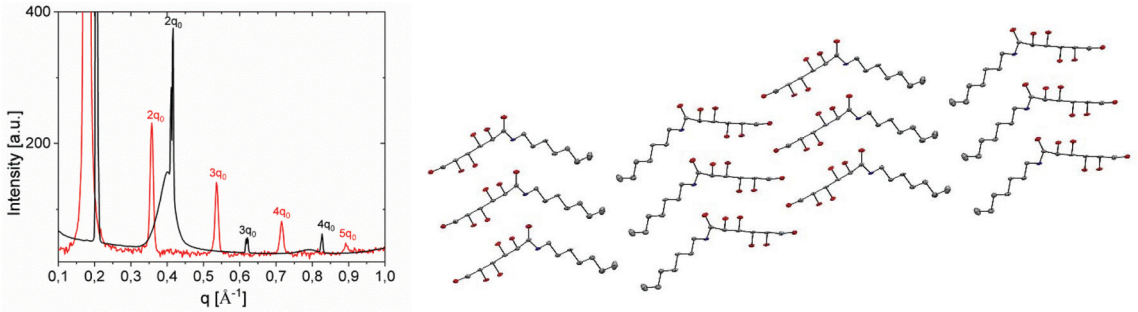

Fig. 9 (a) SAXS spectra of a fresh Gal-C7 wet-spun gel (red curve) and Gal-C7 crystals (black curve). (b) Molecular packing of Gal-C7 in the crystals (H atoms have been omitted for clarity).

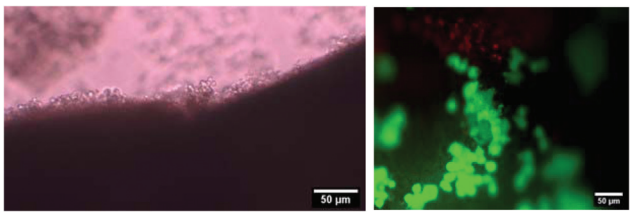

Fig. 10 (a) Neuro2A cells on a gel filament observed directly by bright-field microscopy and (b) Neuro2A cells on a gel filament after live/dead cell staining (3 days of culture). The gel filaments are visible under the cells. Scale bars: 50 μm.

Biocompatibility and filament lifetime under cell culture conditions

The suitability of Gal-C7 gels obtained by wet spinning for cell culture was assessed. For this purpose, the cell viability of a neuronal cell line (Neuro2A) on this material was evaluated with a live–dead cell assay. Overall, the majority of the cells found on the wet-spun gel filament were alive after 3 days. However in all experiments, some dead cells were gathered in some places of the gel (Fig. 10). It looks as if a toxic phenomenon was concentrated in some parts. It means that a lower cell viability is obtained on the wet-spun filaments compared with "bulk gels" on which a cell viability of 98% was obtained.[2] From thermogravimetric measurements, it is found that there is no DMSO left in the wet-spun filaments and, in addition, extensive medium washing processes are performed before cell culture. Thus, it seems unlikely that DMSO induced the toxicity. Alternatively, perhaps other chemical, biochemical or physical factors (fiber size, surface morphology, rigidity, nutrient diffusion *etc.*) may explain this effect. Otherwise, despite the long lifetime observed for the filaments wet-spun in DMEM/FBS at room temperature (part 5), at 37 °C, this lifetime is much reduced. As a consequence, only a few fragments were left after 3 days of culture. The wet-spun gels obtained from Gal-C7 alone are thus too fragile to sustain cell culture and the process has to be improved to get filaments adapted for this application.

Conclusion

In this work, we have shown that wet spinning can be used to organize a low molecular weight gelator into continuous hydrogel filaments with controlled diameters. Moreover, the process led to a high degree of organization of the supramolecular fibers inside the filament: first, the fibers are very homogeneous in size. Secondly, as a result of the radial diffusion of the water inside the liquid rope, they are oriented radially in the filament and are locally aligned. It means that the wet spinning process, applied to this LMWG, enabled better control of its self-assembly as compared to standard procedures based on the cooling of a hot gelator solution. From the point of view of the material properties, the filament obtained is mainly composed of water and can be easily dissolved by simple washing processes. As a consequence, it could be useful as a sacrificial material. The controlled self-assembly of this gelator could alternatively be used in combination with other compounds to organize them in the space. Finally, wet spinning of Gal-C7 could allow the precise deposition of the gel on a surface, opening the way to its application to 3D-printing.

Experimental section

N-Heptyl-D-galactonamide was synthesized according to the procedure described in the study in ref. 2. It can be purchased from Innov'Orga (Reims, France).

Extrusion of the hydrogel filaments

The dope solutions of *N*-heptyl-D-galactonamide were prepared by dissolving the molecule at room temperature in dimethyl sulfoxide (purchased from Fisher, 99%, non-anhydrous) with the help of ultrasound and at different mass concentrations (2.5, 4 or 5 wt%). The solutions were extruded in a bath of ultrapure water (200 mL, bath height of approximately 8 cm) at room temperature (21–23 °C) with a syringe pump (CETONI neMESYS 290N), controlled by the neMESYS UserInterface software. Different gauges of blunt-tip needles, flow rates and concentrations of the solution were used. The videos acquired during these experiments were acquired with a DinoLite

digital microscope (model AM4013MTL-FVW) under white light. Between each condition, the needle was cleaned and the bath was changed to fresh ultrapure water.

Characterization of the solvent exchange

To assess the diffusion of DMSO out of the jet, 1 μm fluorescent beads (FluoSpheres, Invitrogen, diameter of 1 μm, 1.10^{10} beads per ml, ref F13080) were dissolved at 10% in volume in a 4 wt% gelator solution in DMSO. This concentration is sufficient so that the fluorescence is homogeneous in the jet. This resulting solution was then extruded at 50 μl min^{-1} according to the usual wet spinning protocol with a 23G needle (ID of 340 μm). Images were then acquired with two microscope cameras along the jet at different distances after the needle exit, one with white light (DinoLite model AM4013MTL-FVW) and the other with fluorescent light (DinoLite model AM4115T-GFBW, excitation at 480 nm and emission filter at 510 nm). Composite images were then created by overlaying fluorescence images on top of the white light ones with the ImageJ software.

To assess the diffusion of water inside the DMSO jet, 5 mg of salicylaldehyde azine were dissolved into 1 ml of a 4 wt% Gal-C7 solution in DMSO and this solution was extruded at 50 μl min^{-1} with a 20G needle (ID of 600 μm) into a water bath. A video was then taken along the falling jet with the microscope camera suited for fluorescence observations at different distances after the needle exit (DinoLite model AM4115T-GFBW, excitation at 480 nm and emission filter at 510 nm).

Estimation of the jet velocity

For the speed analyses, 15 μm diameter fluorescent beads (purchased from Thermo Fisher Scientific) were used. The beads were suspended in DMSO to reach a concentration suitable for speed analysis (rather low to be able to distinguish the beads with the naked eye in the videos). The suspension was then mixed in the solution of Gal-C7 in DMSO. This last solution was then extruded at 5 or 10 μl min^{-1} and the DMSO jet was filmed with the DinoLite digital microscope suited for fluorescence acquisitions (model AM4115T-GFBW, excitation at 480 nm and emission filter at 510 nm). Three experiments were performed for each flow rate. The velocity was analyzed thanks to the ManualTracking plugin from ImageJ. For 10 μl min^{-1}, a total of 23 beads were tracked throughout the three videos and 30 beads for 5 μl min^{-1}. The measured jet velocity is the mean of the mean velocities of all the analyzed beads ± the associated standard deviation. To obtain the jet diameter under these conditions, several frames of the acquired videos were superimposed, while being careful of taking ones in which the jet was stable. Three different superimpositions at different times were done. The resulting pictures then allowed the measurement of diameters, which were then plotted along the Z axis. The error bars are an estimation of the error made when measuring the diameters (the value of two pixels in the picture, namely 40 μm). The error in the predicted velocity was calculated with the formula: $\Delta v = v(\Delta Q/Q + \Delta d/d)$, with v being the calculated velocity, Q the applied flow rate, ΔQ the error in the flow rate (= 0.00002 mm^3 s^{-1} because the minimal flow that can be applied by the syringe pump is 1 nl min^{-1} with a 1 ml syringe), d the jet diameter and Δd the error in the measured diameter (40 μm).

Measurements of the jet diameters

The jet diameters were measured from several snapshots from the videos of the extrusion. The videos were acquired with the DinoLite digital microscope (model AM4013MTL-FVW) under white light and with maximum magnification. The extrusions were recorded for approximately 2 min and snapshots of the videos were further taken around every 30 s. The jet diameters were then measured from these snapshots with ImageJ, at a distance of 2.3 mm after the extremity of the needle (maximum distance considering the picture size). The mean and standard deviation of the measured diameters were then calculated for each condition.

Optical transmission microscopy of the filaments

For microscopic observations, the wet-spun gel filaments were retrieved thanks to a sieve in which a circular microscope slide was placed and plunged into the bath. The diameters of the wet-spun filaments were measured by transmission optical microscopy on an Olympus inverted microscope (bright field, ×10). At least three pictures at different points of the filament were taken for each condition and the mean and standard error of the diameters (measured with ImageJ) were calculated.

Cryo-SEM observations

Gel filaments were prepared according to the wet spinning previously described and retrieved thanks to a sieve placed in the coagulation bath. The most robust filaments, corresponding to the conditions: 4 wt%; 50 μl min^{-1} (Fig. 4c) and 5 wt%; 50 μl min^{-1} (Fig. 4d), were studied. A part of the gel filament was then deposited on the cryo-SEM cane and frozen at −220 °C in liquid nitrogen. The frozen sample was fractured at −145 °C under vacuum in a cryo-transfer system chamber (Quorum PP3000 T). The sublimation was performed at −95 °C for 30 min. The sample was metalized with Pd for 60 s and introduced in the microscope. The temperature was kept at −145 °C. Images were recorded with an FEG FEI Quanta 250 microscope, at 5 kV for the acceleration voltage. Some of them with a suitable magnification and orientation (around 10 to 20 measures per gel) provided a rough estimation of the fiber thickness.

Thermo-gravimetric analysis

Gal-C7 gel filaments were prepared by wet spinning: they were extruded at 50 μl min^{-1} with a 4 wt% solution of Gal-C7 in DMSO and a 20G blunt-tip needle. A sieve was placed at the bottom of the water tank to retrieve the formed filaments. The filaments were kept in the sieve in a very small volume of water for one hour before measurement. About ten milligrams of filaments were then placed in a crucible and the water surrounding the filaments was wiped off before analysis. The

temperature program was as follows: heating from 30.00 °C to 300.00 °C at 1.00 °C min^{-1}, then heating from 300.00 °C to 600.00 °C at 10.00 °C min^{-1} and holding for 10.0 min at 600.00 °C (under nitrogen, 100.0 ml min^{-1}). The composition of the gel was then calculated as follows: the mass of each component was measured between the plateaus on the curve and the percentage of the total initial mass was then calculated. TGA was also performed with the Gal-C7 solid alone (Fig. SI-2b†) and with a solution of 1 wt% DMSO in pure water (Fig. SI-2c†) as references.

Study of the lifetime of the filaments in solutions

30 µl of Gal-C7 in DMSO (4 wt%) were extruded in approximately 200 ml of ultrapure water (≈8 cm of fall), with a 20G needle at 50 µL min^{-1}, and the resulting filaments were retrieved thanks to a glass slide placed in a sieve at the bottom of the water tank. After spinning, the glass slide was rapidly put in a well of a 12-well cell culture plate and 1 ml of the different solutions (ultrapure water, PBS (Phosphate Buffer Saline) 10×, or DMEM (Dulbecco's Modified Eagle's medium) supplemented with 10% FBS (Fetal Bovine Serum) and 1% penicillin–streptomycin) was added inside the well. In some cases, another glass slide was put on top of the liquid while being careful to not let it sink in the liquid (an air bubble keeps the slide from sinking). The plate was then kept either at room temperature (21–23 °C) or at 37 °C in a stove in the case of trials with DMEM. The filaments were then observed every day by optical microscopy (upright Olympus microscope, bright field, ×5 or ×10). At least five different pictures were taken for each well. The diameters of the resulting fibers were then manually measured with the ImageJ software and the mean and standard deviation were calculated for each day.

Small angle X-ray scattering (SAXS)

Scattering measurements were performed on freshly wet-spun gels of Gal-C7 obtained from a 5 wt% DMSO solution extruded at 25 µl min^{-1}. Crystals were obtained from wet-spun filaments obtained from a 2.5 wt% DMSO solution extruded at 25 µl min^{-1} and aged for two weeks. A XEUSS 2.0 SAXS/WAXS laboratory beamline equipped with a Cu source (E = 8 keV) and a pixel detector PILATUS3 1 M from Detrics was used. The sample-to-detector distance was 0.387 m (beam size: 0.8 mm × 0.8 mm) allowing a q range between 0.022 $Å^{-1}$ and 1.6 $Å^{-1}$. Samples were mounted on a sample holder for gels with a kapton window. Measurements were carried out at 25 °C.

Crystallographic data collection and structure determination for Gal-C7

The data were collected at low temperature (193 K) on a Bruker-AXS APEX II QUAZAR diffractometer equipped with a 30 W air-cooled microfocus source, using MoKα radiation (λ = 0.71073 Å). Phi- and omega-scans were used. The data were integrated with SAINT, and an empirical absorption correction with SADABS was applied.[83] The structure was solved by direct methods (ShelXT)[84] and refined using the least-squares method on F^2 (ShelXL).[85] All non-H atoms were refined with anisotropic displacement parameters. The H atoms were refined isotropically at calculated positions using a riding model, except on oxygen and nitrogen atoms. These H atoms were located by a difference Fourier map. Selected data for Gal-C7: $C_{13}H_{27}NO_6$, M = 293.35, monoclinic, space group $P2_1$, a = 4.957(3) Å, b = 5.007(4) Å, c = 30.60(2) Å, β = 92.980(8)°, V = 758.4(9) $Å^3$, Z = 2, crystal size: 0.40 × 0.20 × 0.01 mm^3, 14 967 reflections collected (3063 independent, R_{int} = 0.1024), 204 parameters, 1 restraint, R_1 [$I > 2\sigma(I)$] = 0.0784, wR_2 [all data] = 0.1680, largest diff. peak and hole: 0.345 and −0.294 e $Å^{-3}$.

Cell culture assays

100 µl of a 4 wt% Gal-C7 solution in DMSO were extruded according to the previously described protocol in a bath of sterile water and with a sterile syringe and needle. The gel filaments were transferred into the wells of a 12-well cell culture plate. The filaments were then rinsed 3 times (for 2 hours, overnight and 4 hours) with 2 ml of DMEM (Dulbecco's modified Eagle's medium) supplemented with 10% fetal bovine serum and 1% penicillin–streptomycin at room temperature. 50 000 cells of a neuronal cell line (Neuro2A, ATCC) were then seeded on the scaffolds with 2 mL of cell culture medium and incubated for 3 days at 37 °C under a humidified atmosphere containing 5% CO_2. Fluorescence live–dead staining assay (Molecular probe) was used according to the manufacturer's instructions to visualize the proportion of viable cells in green (calcein AM) and nonviable cells in red (ethidium homodimer-1). The samples were observed using a Zeiss Axioskop microscope equipped with a Cool SNAPfx camera (Photometrics).

Conflicts of interest

There are no conflicts to declare.

Acknowledgements

We acknowledge Christophe Coudret for the kind gift of salicylaldehyde azine and helpful discussion about molecules with aggregation induced emission; Pierre Roblin (IR, CNRS, LGC Toulouse) for support in SAXS measurements and FR FERMAT, Université de Toulouse, France-CPER IMATECBIO and for providing access to SAXS instrument XEUSS 2.0 XENOCS; and Bruno Payré, Isabelle Fourquaux, Dominique Goudounèche from CMEAB "Centre de Microscopie Electronique Appliquée à la Biologie" for TEM and cryo-TEM. This work was supported by the French National Research Agency (A. C.'s grant and financial support, ANR "Neuraxe", grant N°ANR-15-CE07-0007-01) and as part of the MultiFAB project which has received funding from FEDER European Regional Funds and Région Occitanie – France (Grant Number: 16007407/MP0011594). The European Union is also acknowledged for its financial support for equipment (FEDER-35477: "Nano-objets pour la biotechnologie").

References

1 G.-F. Liu, D. Zhang and C.-L. Feng, *Angew. Chem., Int. Ed.*, 2014, **53**, 7789–7793.
2 A. Chalard, L. Vaysse, P. Joseph, L. Malaquin, S. Souleille, B. Lonetti, J.-C. Sol, I. Loubinoux and J. Fitremann, *ACS Appl. Mater. Interfaces*, 2018, **10**, 17004–17017.
3 J. Zhou, J. Li, X. Du and B. Xu, *Biomaterials*, 2017, **129**, 1–27.
4 K. J. Skilling, F. Citossi, T. D. Bradshaw, M. Ashford, B. Kellam and M. Marlow, *Soft Matter*, 2014, **10**, 237–256.
5 X. Du, J. Zhou, J. Shi and B. Xu, *Chem. Rev.*, 2015, **115**, 13165–13307.
6 X.-Q. Dou and C.-L. Feng, *Adv. Mater.*, 2017, 1604062.
7 M. J. Webber, E. A. Appel, E. W. Meijer and R. Langer, *Nat. Mater.*, 2015, **15**, 13–26.
8 S. Koutsopoulos, *J. Biomed. Mater. Res., Part A*, 2016, **104**, 1002–1016.
9 V. M. P. Vieira, A. C. Lima, M. de Jong and D. K. Smith, *Chem. – Eur. J.*, 2018, **24**, 15112–15118.
10 T. Tsuzuki, M. Kabumoto, H. Arakawa and M. Ikeda, *Org. Biomol. Chem.*, 2017, **15**, 4595–4600.
11 I. S. Okafor and G. Wang, *Carbohydr. Res.*, 2017, **451**, 81–94.
12 Y. Ohsedo, M. Oono, K. Saruhashi and H. Watanabe, *RSC Adv.*, 2014, **4**, 48554–48558.
13 S. Datta and S. Bhattacharya, *Chem. Soc. Rev.*, 2015, **44**, 5596–5637.
14 X. Xiao, J. Hu, X. Wang, L. Huang, Y. Chen, W. Wang, J. Li and Y. Zhang, *Chem. Commun.*, 2016, **52**, 12517–12520.
15 N. Baccile, L. V. Renterghem, P. L. Griel, G. Ducouret, M. Brennich, V. Cristiglio, S. L. K. W. Roelants and W. Soetaert, *Soft Matter*, 2018, **14**, 7859–7872.
16 M. Kamada, C. Pierlot, V. Molinier, J.-M. Aubry and K. Aramaki, *Colloids Surf., A*, 2018, **536**, 82–87.
17 L. Latxague, M. A. Ramin, A. Appavoo, P. Berto, M. Maisani, C. Ehret, O. Chassande and P. Barthélémy, *Angew. Chem., Int. Ed.*, 2015, **54**, 4517–4521.
18 M. G. F. Angelerou, P. W. J. M. Frederix, M. Wallace, B. Yang, A. Rodger, D. J. Adams, M. Marlow and M. Zelzer, *Langmuir*, 2018, **34**, 6912–6921.
19 K. J. Skilling, B. Kellam, M. Ashford, T. D. Bradshaw and M. Marlow, *Soft Matter*, 2016, **12**, 8950–8957.
20 J. Baillet, V. Desvergnes, A. Hamoud, L. Latxague and P. Barthélémy, *Adv. Mater.*, 2018, **30**, 1705078.
21 M. A. Ramin, L. Latxague, K. R. Sindhu, O. Chassande and P. Barthélémy, *Biomaterials*, 2017, **145**, 72–80.
22 L. Latxague, A. Gaubert and P. Barthélémy, *Molecules*, 2018, **23**, 89.
23 D. Yuan, X. Du, J. Shi, N. Zhou, A. A. Baoum, K. O. A. Footy, K. O. Badahdah and B. Xu, *Beilstein J. Org. Chem.*, 2015, **11**, 1352–1359.
24 T. Das, M. Häring, D. Haldar and D. Díaz Díaz, *Biomater. Sci.*, 2018, **6**, 38–59.
25 D. Tarus, L. Hamard, F. Caraguel, D. Wion, A. Szarpak-Jankowska, B. van der Sanden and R. Auzély-Velty, *ACS Appl. Mater. Interfaces*, 2016, **8**, 25051–25059.
26 A. Li, A. Hokugo, A. Yalom, E. J. Berns, N. Stephanopoulos, M. T. McClendon, L. A. Segovia, I. Spigelman, S. I. Stupp and R. Jarrahy, *Biomaterials*, 2014, **35**, 8780–8790.
27 C. Davoust, B. Plas, A. Béduer, B. Demain, A.-S. Salabert, J. C. Sol, C. Vieu, L. Vaysse and I. Loubinoux, *Stem Cell Res. Ther.*, 2017, **8**, 253.
28 L. Vaysse, F. Conchou, B. Demain, C. Davoust, B. Plas, C. Ruggieri, M. Benkaddour, M. Simonetta-Moreau and I. Loubinoux, *Behav. Neurosci.*, 2015, **129**, 423–434.
29 J. Fitremann, B. Lonetti, E. Fratini, I. Fabing, B. Payré, C. Boulé, I. Loubinoux, L. Vaysse and L. Oriol, *J. Colloid Interface Sci.*, 2017, **504**, 721–730.
30 E. R. Draper, O. O. Mykhaylyk and D. J. Adams, *Chem. Commun.*, 2016, **52**, 6934–6937.
31 B. D. Wall, S. R. Diegelmann, S. Zhang, T. J. Dawidczyk, W. L. Wilson, H. E. Katz, H.-Q. Mao and J. D. Tovar, *Adv. Mater.*, 2011, **23**, 5009–5014.
32 S. Zhang, M. A. Greenfield, A. Mata, L. C. Palmer, R. Bitton, J. R. Mantei, C. Aparicio, M. O. de la Cruz and S. I. Stupp, *Nat. Mater.*, 2010, **9**, 594–601.
33 Q. Tong, L. Zhang, Y. Li, B. Li and Y. Yang, *Soft Matter*, 2018, **14**, 6353–6359.
34 I. Ziemecka, G. J. M. Koper, A. G. L. Olive and J. H. van Esch, *Soft Matter*, 2013, **9**, 1556–1561.
35 M. Numata, *Chem. – Asian J.*, 2015, **10**, 2574–2588.
36 D. Hermida-Merino, M. Trebbin, S. Foerster, F. Rodriguez-Llansola and G. Portale, *Macromol. Symp.*, 2015, **358**, 59–66.
37 D. Kiriya, M. Ikeda, H. Onoe, M. Takinoue, H. Komatsu, Y. Shimoyama, I. Hamachi and S. Takeuchi, *Angew. Chem., Int. Ed.*, 2012, **51**, 1553–1557.
38 M. Numata, R. Nogami and A. Kitamura, *ChemNanoMat*, 2018, **4**, 175–182.
39 S. Tamaru, M. Ikeda, Y. Shimidzu, S. Matsumoto, S. Takeuchi and I. Hamachi, *Nat. Commun.*, 2010, **1**, 20.
40 R. Contreras-Montoya, A. B. Bonhome-Espinosa, A. Orte, D. Miguel, J. M. Delgado-López, J. D. G. Duran, J. M. Cuerva, M. T. Lopez-Lopez and L. Á. de Cienfuegos, *Mater. Chem. Front.*, 2018, **2**, 686–699.
41 P. van der Asdonk, M. Keshavarz, P. C. M. Christianen and P. H. J. Kouwer, *Soft Matter*, 2016, **12**, 6518–6525.
42 C. Vigier-Carrière, F. Boulmedais, P. Schaaf and L. Jierry, *Angew. Chem., Int. Ed.*, 2018, **57**, 1448–1456.
43 J. Rodon Fores, M. L. Martinez Mendez, X. Mao, D. Wagner, M. Schmutz, M. Rabineau, P. Lavalle, P. Schaaf, F. Boulmedais and L. Jierry, *Angew. Chem., Int. Ed.*, 2017, **56**, 15984–15988.
44 M. G. F. Angelerou, B. Yang, T. Arnold, J. Rawle, M. Marlow and M. Zelzer, *Soft Matter*, 2018, **14**, 9851–9855.
45 L. Fan, J.-L. Li, Z. Cai and X. Wang, *ACS Nano*, 2018, **12**, 5780–5790.

46 Y. Dou, B. Wang, M. Jin, Y. Yu, G. Zhou and L. Shui, *J. Micromech. Microeng.*, 2017, **27**, 113002.
47 M. Numata, Y. Takigami, M. Takayama, T. Kozawa and N. Hirose, *Chem. – Eur. J.*, 2012, **18**, 13008–13017.
48 A. Yaari, Y. Schilt, C. Tamburu, U. Raviv and O. Shoseyov, *ACS Biomater. Sci. Eng.*, 2016, **2**, 349–360.
49 K. D. Nelson, A. Romero, P. Waggoner, B. Crow, A. Borneman and G. M. Smith, *Tissue Eng.*, 2003, **9**, 1323–1330.
50 K. Tuzlakoglu, I. Pashkuleva, M. T. Rodrigues, M. E. Gomes, G. H. van Lenthe, R. Müller and R. L. Reis, *J. Biomed. Mater. Res., Part A*, 2010, **92**, 369–377.
51 Y. Yang, X. Liu, D. Wei, M. Zhong, J. Sun, L. Guo, H. Fan and X. Zhang, *Biofabrication*, 2017, **9**, 045009.
52 S. Hirano, *Macromol. Symp.*, 2001, **168**, 21–30.
53 M. Desorme, A. Montembault, T. Tamet, P. Maleysson, T. Bouet and L. David, *J. Appl. Polym. Sci.*, 2019, **136**, 47130.
54 B. R. Lee, K. H. Lee, E. Kang, D.-S. Kim and S.-H. Lee, *Biomicrofluidics*, 2011, **5**, 022208.
55 R. Madurga, A. M. Gañán-Calvo, G. R. Plaza, G. V. Guinea, M. Elices and J. Pérez-Rigueiro, *Green Chem.*, 2017, **19**, 3380–3389.
56 N. Weatherbee-Martin, L. Xu, A. Hupe, L. Kreplak, D. S. Fudge, X.-Q. Liu and J. K. Rainey, *Biomacromolecules*, 2016, **17**, 2737–2746.
57 Y. Hsia, E. Gnesa, R. Pacheco, K. Kohler, F. Jeffery and C. Vierra, *J. Visualized Exp.*, 2012, **65**, e4191.
58 J. Cheng, Y. Jun, J. Qin and S.-H. Lee, *Biomaterials*, 2017, **114**, 121–143.
59 C. Mota, S.-Y. Wang, D. Puppi, M. Gazzarri, C. Migone, F. Chiellini, G.-Q. Chen and E. Chiellini, *J. Tissue Eng. Regener. Med.*, 2017, **11**, 175–186.
60 D. Puppi, C. Migone, A. Morelli, C. Bartoli, M. Gazzarri, D. Pasini and F. Chiellini, *J. Bioact. Compat. Polym.*, 2016, **31**, 531–549.
61 S. M. Hashemnejad and S. Kundu, *Langmuir*, 2017, **33**, 7769–7779.
62 R. V. Bell, C. C. Parkins, R. A. Young, C. M. Preuss, M. M. Stevens and S. A. F. Bon, *J. Mater. Chem. A*, 2016, **4**, 813–818.
63 M. Hecht, B. Soberats, J. Zhu, V. Stepanenko, S. Agarwal, A. Greiner and F. Würthner, *Nanoscale Horiz.*, 2018, **4**, 169–174.
64 M. Maleki, A. Natalello, R. Pugliese and F. Gelain, *Acta Biomater.*, 2017, **51**, 268–278.
65 G. Singh, A. M. Bittner, S. Loscher, N. Malinowski and K. Kern, *Adv. Mater.*, 2008, **20**, 2332–2336.
66 M. Allais, D. Mailley, P. Hébraud, D. Ihiawakrim, V. Ball, F. Meyer, A. Hébraud and G. Schlatter, *Nanoscale*, 2018, **10**, 9164–9173.
67 A. Celebioglu, F. Topuz, Z. I. Yildiz and T. Uyar, *Carbohydr. Polym.*, 2019, **207**, 471–479.
68 H. Yoshida, K. Kikuta and T. Kida, *Beilstein J. Org. Chem.*, 2019, **15**, 89–95.
69 M. G. McKee, J. M. Layman, M. P. Cashion and T. E. Long, *Science*, 2006, **311**, 353–355.
70 M. Habibi, N. M. Ribe and D. Bonn, *Phys. Rev. Lett.*, 2007, **99**, 154302.
71 E. R. Draper, T. O. McDonald and D. J. Adams, *Chem. Commun.*, 2015, **51**, 6595–6597.
72 W. Liyanage, W. W. Brennessel and B. L. Nilsson, *Langmuir*, 2015, **31**, 9933–9942.
73 Y. Wang, L. Tang and J. Yu, *Cryst. Growth Des.*, 2008, **8**, 884–889.
74 B. P. Krishnan and K. M. Sureshan, *ChemPhysChem*, 2016, **17**, 3062–3067.
75 J. Liu, F. Xu, Z. Sun, Y. Pan, J. Tian, H.-C. Lin and X. Li, *Soft Matter*, 2016, **12**, 141–148.
76 D. Krishna Kumar and J. W. Steed, *Chem. Soc. Rev.*, 2014, **43**, 2080–2088.
77 K. A. Houton, K. L. Morris, L. Chen, M. Schmidtmann, J. T. A. Jones, L. C. Serpell, G. O. Lloyd and D. J. Adams, *Langmuir*, 2012, **28**, 9797–9806.
78 J. H. Fuhrhop, P. Schnieder, E. Boekema and H. Wolfgang, *J. Am. Chem. Soc.*, 1988, **110**, 2861–2867.
79 C. André, P. Luger and S. Svenson, *Carbohydr. Res.*, 1992, **230**, 31–40.
80 C. André, P. Luger, S. Svenson and J.-H. Fuhrhop, *Carbohydr. Res.*, 1993, **240**, 47–56.
81 V. Zabel, A. Müller-Fahrnow, R. Hilgenfeld, W. Saenger, B. Pfannemüller, V. Enkelmann and W. Welte, *Chem. Phys. Lipids*, 1986, **39**, 313–327.
82 S. M. Hashemnejad, M. M. Huda, N. Rai and S. Kundu, *ACS Omega*, 2017, **2**, 1864–1874.
83 *SADABS, Program for Data Correction*, Bruker-AXS.
84 G. M. Sheldrick, *Acta Crystallogr., Sect. A: Found. Adv.*, 2015, **71**, 3–8.
85 G. M. Sheldrick, *Acta Crystallogr., Sect. C: Struct. Chem.*, 2015, **71**, 3–8.

